

Symmetry-dependent antiferromagnetic proximity effects on valley splitting

Chengyang Xu,¹ Lingxian Kong², and Weidong Luo^{1,3,*}

¹Key Laboratory of Artificial Structures and Quantum Control (Ministry of Education), School of Physics and Astronomy, Shanghai Jiao Tong University, Shanghai 200240, China

²International Center for Quantum Materials, School of Physics, Peking University, Beijing 100871, China

³Institute of Natural Sciences, Shanghai Jiao Tong University, Shanghai 200240, China



(Received 16 August 2022; revised 31 January 2023; accepted 24 February 2023; published 13 March 2023)

Various physical phenomena have been discovered by tuning degrees of freedom, among which there is the “valley” degree of freedom (DOF). The typical valley materials are characterized by two degenerate valley states protected by time-reversal symmetry (TS). These states indexed by valley DOF have been measured and manipulated for emergent valley-contrasting physics with the broken valley degeneracy. To achieve the valley splitting resulting from TS breaking, previous studies have mainly focused on the magnetic proximity effect provided by the ferromagnetic layer. In contrast, the antiferromagnetic (AFM) proximity effect on the valley degeneracy has not been widely investigated systematically. In this work, we construct the composite systems consisting of a transition-metal dichalcogenide monolayer and a proximity layer with specific intraplane AFM configurations. We extend the three-band model to describe the valley states of such systems. It is shown that either “time-reversal + fractional translation” or “mirror” symmetry can protect the valley degeneracy. Additionally, first-principles calculations based on density functional theory (DFT) have been performed to verify the results obtained from the extended tight-binding (TB) model. The corresponding mechanism of the valley splitting/degeneracy is revealed through the nondegenerate perturbation. Meanwhile, an extra condition is proposed to keep the well-defined valley states disentangled from each other through two negative examples based on degenerate perturbation. Further DFT studies on the effects of the U_{eff} and interlayer distance are performed. Manipulating the magnetization of Mo is shown to be feasible and effective for controlling the valley splitting with the direct overlap tuned by U_{eff} and the interlayer distance. The TB method introduced in the present work can properly describe the low-energy physics of valley materials that couple to the proximity with complex magnetic configurations. The results considerably expand the range of qualified proximity layers for valley splitting, enabling more flexible manipulation of valley degree.

DOI: [10.1103/PhysRevB.107.125408](https://doi.org/10.1103/PhysRevB.107.125408)

I. INTRODUCTION

Two-dimensional (2D) systems provide ideal platforms for exploring physical phenomena by modifying different degrees of freedom (DOF). In some 2D materials, especially the H-phase monolayer transition-metal dichalcogenides (TMDs), there is the “valley” DOF for electrons in the low-energy region [1–4]. As the first proposed monolayer in the TMD family, strong valley-selective photoluminescence in directly gapped MoS₂ was observed with optical pumping [5,6]. Subsequent investigations into valley-contrasting physical quantities have been reported in many other TMDs (e.g., MoSe₂, WS₂, and WSe₂). Electrons with different valley indices can be controllably excited through the helicity of light [3,7]. With in-plane electric field, the valley degree can be detected through the valley Hall effects, where carriers at different valleys transport along opposite boundaries [1,8]. Analogous to spintronics, electronic valley as an information carrier may open up a new paradigm for data processing and

storage based on the understanding and precise control of the valley DOF [9,10].

As an intrinsic nature of materials, the valley degree is strongly related to the symmetry of the system. One of the most promising 2D materials for manipulating the valley degree is the H-phase monolayer TMDs with the direct gap locating at the corners of the hexagonal Brillouin zone (BZ). This triangular-type lattice consists of pristine cells with one transition-metal (M) atom centered in the prism formed by the nearest chalcogen (X) atoms, as shown in Figs. 1(a) and 1(b). The loss of inversion symmetry and strong spin-orbit coupling lead to the spin-valley coupled states at the band edges K and $-K$. The corresponding spin orientation at the two valleys is opposite due to the time-reversal symmetry, as schematically shown in Fig. 1(d). This spin-valley locking relationship is the key to the observable effects such as the valley Hall effect [8], valley-contrasting circular dichroism [4], and valley-selective excitation of excitonic states [5,11,12].

Recently, lifting the valley degeneracy protected by TS has been implemented for precise control of the valley effects in such monolayer TMDs. An external magnetic field was utilized to induce a small valley splitting of 0.1–0.2 meV/T in previous works [13–15]. In comparison, the

*wdluo@sjtu.edu.cn

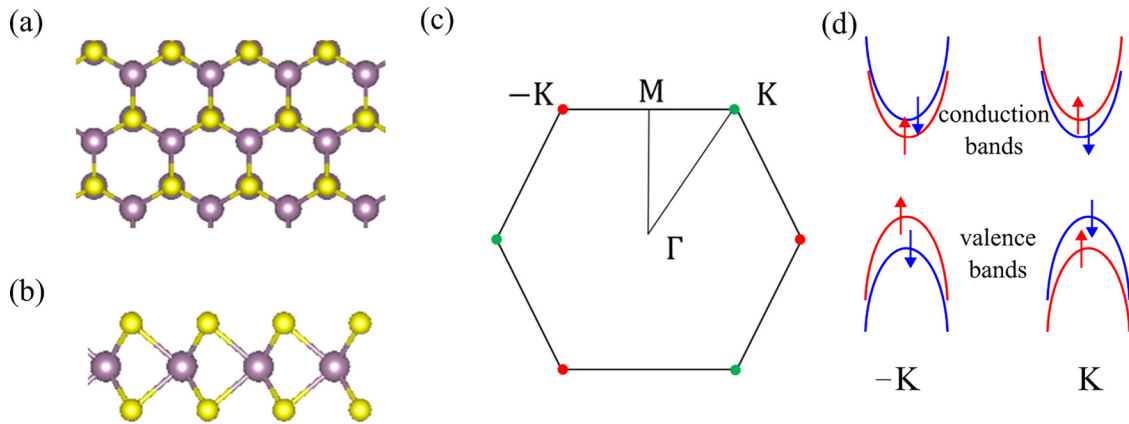


FIG. 1. (a),(b) Top and side views of the valley material monolayer TMD MX_2 ($M = \text{Mo}, \text{W}$; $X = \text{S}, \text{Se}$). The purple/yellow spheres denote the M/X atoms. (c) Brillouin zone and high-symmetry points of monolayer TMD, with red and green points denoting the two valleys. (d) Schematic conduction and valence bands of MX_2 at two valleys. Spin up and spin down are denoted by red and blue arrows, respectively. The spin orientations of the two eigenstates with the same energy are opposite at K and $-K$ due to the \mathcal{TS} .

magnetic proximity effect could generate giant valley splitting, increasing by an order of magnitude to several meV/T, in semiconductor/ferromagnet hybrids [16–18]. A sizable valley splitting also occurs under the antiferromagnetic (AFM) proximity effect with an A-type configuration [19]. And the exchange field was found to be dominated by the interfacial magnetic layer, where the magnetic moments are ferromagnetic (FM) coupling. Hence, the proximity effect is still limited to the case of the FM type.

So far, it is still unclear whether intraplane AFM proximity would result in the valley splitting of TMD monolayers. The systems seem to be valley degenerate under the intraplane AFM proximity effect since the exchange field over the whole magnetic unit cell is zero. However, the orbital-dependent exchange paths and distance-dependent magnetic exchange yield a nonzero effective Zeeman splitting for each atom. Thus, it is hard to determine whether the valley degeneracy breaks in terms of the overall effective exchange field. Yet, the symmetry of the proximity layer offers an effective method to analyze the problem. If the valley degeneracy remains under the magnetic proximity effect, there must exist at least one symmetry that relates the two states featured by (K, σ) and $(-K, \bar{\sigma})$.

In the present paper, we start from the symmetries that can reverse the spin and momentum simultaneously. Three special AFM configurations are constructed in Sec. II A. In Sec. II B, the MoTe_2 monolayer has been adopted as the TMD layer. A three-band TB model is extended with an additional term to study the proximity effects of the three specific AFM configurations. In Sec. II C, first-principles density functional theory (DFT) calculations are carried out to validate the TB results. In Sec. III A, the vertical “mirror” (σ_v) symmetry in the type II and the “time-reversal + fractional translation” (\mathcal{T}_{tr}) symmetry in type I are shown to protect the valley degeneracy through the symmetry analysis. And the valley splitting appears as predicted in type III, exhibiting the dependence on the orbital-resolved exchange field. In Sec. III B, the nondegenerate perturbation theory is adopted to explain the mechanism of the valley splitting/degeneracy in the three types of AFM configurations. In order to preserve the

well-defined valley states, another two special configurations, types IV and V, are constructed as the negative examples. These two configurations are featured by the reciprocal lattice vectors through which K and $-K$ fold to the same point. Based on the degenerate perturbation theory, the constraints of the AFM configurations are obtained. In Sec. III C, the dependence of the valley splitting on the interlayer distance and U_{eff} parameter has been studied through the DFT calculations. A larger valley splitting is induced with a larger overlap between orbitals of the M atoms and the magnetic ones. The magnetization of the M atom is found to be the key factor tuned through the interlayer distance and U_{eff} .

II. METHODS

A. Symmetry analysis for constructing AFM configurations

The degenerate valley states refer to the two states, indexed by different valleys, holding the same eigenenergy nonaccidentally. In MX_2 (Fig. 1), the valleys locate at K and $-K$ where bands reach the valence-band maximum and conduction-band minimum. The \mathcal{TS} resulting from the nonmagnetism protects the Kramers’ degeneracy of the two states specified by opposite momentum and spin orientation. When the magnetic proximity effect is introduced, the \mathcal{TS} is broken. If the normal degeneracy of valley states remains, at least one common symmetry other than \mathcal{TS} of the TMD monolayer and proximity layer reverses the momentum and spin indexes of the valley states.

Based on the symmetry analysis above, two hypothetical AFM configurations are constructed in Figs. 2(a) and 2(b). The configuration in Fig. 2(a) keeps the \mathcal{T}_{tr} symmetry. After the intraplane AFM proximity is taken into account, the enlarged unit cell including two magnetic atoms in real space corresponds to a downsized irreducible BZ, shown in Fig. 7(a). Note that the fractional translation of the periodic AFM configuration is a linear combination of integer multiples of the lattice vectors of the MX_2 . The \mathcal{T}_{tr} converts the red points (sites with net spin up) to the green ones (sites with net spin down) through the t_{tr} and then swaps them again with \mathcal{T} . The other configuration [Fig. 2(b)] holds the σ_v symmetry,

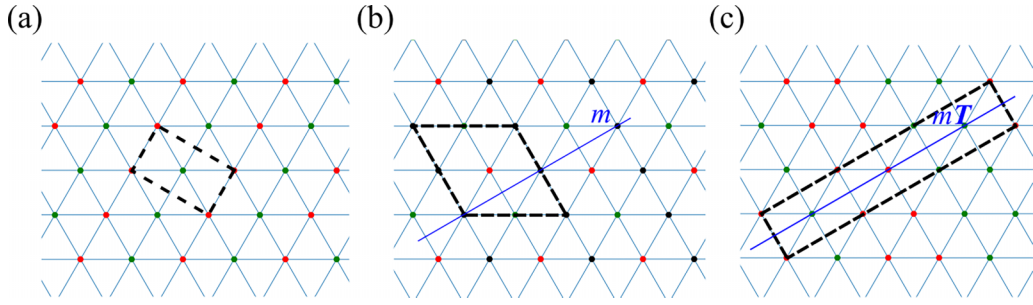


FIG. 2. (a)–(c) Type I–III intraplane AFM configurations. Red/green points denote the nearest-neighbor exchange field provided by the spin magnetic moment \uparrow/\downarrow . The spin-quantization axis is normal to the layer. Black points denote the nonproximity effect at the corresponding sites. Black dashed lines denote the unit cell after intraplane AFM proximity is introduced. (b) Type II is symmetric about the vertical mirror plane labeled by the blue line. (c) Type III is unchanged under the vertical mirror symmetry combined with \mathcal{TS} , which is not the group element of the TMD layer.

enabling the flipping of the spin z component. The 2×2 construction of the unit cell generates a smaller hexagonal BZ without any rotation, as shown in Fig. 7(b). Both AFM configurations in Figs. 2(a) and 2(b) are expected to keep the valley degeneracy. It is worth mentioning that both magnetic configurations of type I and type II hold the “inversion” symmetry. However, when they couple to the TMD monolayer, the inversion symmetry will never be the group element of the whole system. On the other hand, the configuration with neither \mathcal{T}_R or σ_v symmetry [Fig. 2(c)] is considered as well. It aims to illustrate that the absence of the nontrivial symmetries of the coupled system is responsible for valley splitting. For abbreviation, the valley splitting in the following parts refers to the splitting of the two degenerate valley states defined in the TMD monolayer. It is quantified by the energy difference of the top valence band at K and $-K$, which is given by $\Delta_{rvb} = E_{rvb}(K, \downarrow) - E_{rvb}(-K, \uparrow)$. The splitting of the lowest conduction band at two valleys is not included since the results and analyses follow the same pattern.

B. Tight-binding model

Generally speaking, valley degeneracy or splitting is confirmed by eigenvalues of the bands at two valleys. Based on a three-band TB model for monolayer TMDs [20], the conduction and valence bands at the $\pm K$ valleys are well described in the minimal basis composed of Mo $\{d_{z^2}, d_{xy}, d_{x^2-y^2}\}$. The three-band Hamiltonian is expressed as [20]

$$H_0 = \sum_{i,\alpha,\beta,\sigma} \mu_{\alpha\beta} c_{i\alpha\sigma}^\dagger c_{i\beta\sigma} + \sum_{i,j,\alpha,\beta,\sigma} h_{ij}^{\alpha\beta} c_{i\alpha\sigma}^\dagger c_{j\beta\sigma}, \quad (1)$$

with $\alpha(\beta)$, σ denoting orbital and spin indices. And i, j represent neighboring lattice sites. It should be noted that the on-site energy matrix $\mu_{\alpha\beta}$ is not diagonal because of the spin-orbit coupling. With the D_{3h} point group taken into account, the number of independent parameters reduces to nine. In this work, the TB model is parameterized from the MoTe₂ monolayer [20]. The band structure from this model is consistent with the DFT calculation as shown in Figs. 3(c) and 3(d).

To involve the intraplane AFM proximity effect, the effective exchange field provided by the magnetic proximity is treated as a staggered on-site energy modifier term [21], which

is given by

$$H' = \sigma_z \sum_{i,\alpha,\sigma} O_{i\alpha} c_{i\alpha\sigma}^\dagger c_{i\alpha\sigma}. \quad (2)$$

This diagonal on-site correction $O_{i\alpha}$ represents the energy shift of orbital α at lattice site i . The unfolded bands are required to remain the main features under $\vec{O}_i \neq \vec{0}$ such that the proximity effect could be viewed as a perturbation to the three-band model. The orbital-resolved exchange fields provided by the spin-up and spin-down magnetic moment are opposite with $-\vec{O}_G = \vec{O}_R = \vec{O}$, as shown in Fig. 2. The zero matrix $\vec{O}_B = (0, 0, 0)$ eV acts on the nonproximity sites, denoted by black circles in Fig. 2.

The band structures of the coupled systems are accessible with the extended three-band Hamiltonian $H = H_0 + H'$. The enlarged unit cell results in a smaller BZ and more bands from the folding process, which increases the difficulty of locating the original valley states. For clarity, effective bands in the primitive BZ are obtained via the unfolding technique [22–25], with the unfolding projection weight $W_{\mathbf{K} \rightarrow \mathbf{k}} = \langle \mathbf{K} | \mathcal{P}_{\mathbf{k}} | \mathbf{K} \rangle$ [24].

C. First-principles calculations

We perform the first-principles calculations using the Vienna Ab initio Simulation Package (VASP) [26,27] with the projector augmented-wave (PAW) method [28] and Perdew-Burke-Ernzerhof (PBE) functional [29,30] of the generalized-gradient approximation. In addition to spin-orbit coupling, correction of the Hubbard U with the rotationally invariant approach for interacting localized Mn $3d$ orbitals [31] is included in the calculations. The magnetic moments are forced to align perpendicular to the layer. Based on the DFT results, the postprocessed band unfolding calculation is carried out with the plane-wave basis method [23].

With 1H-type MoTe₂ as the TMD layer, the MnO (111) monolayer terminated with Mn atoms right below Mo atoms is taken as the proximity layer for two reasons: (i) The additional bands are disentangled from the original valley states within the low-energy region. (ii) The effective magnetic field from the half-filled $3d$ orbitals of Mn²⁺ acts on all $4d$ orbitals of Mo. A sizable valley splitting in the case of the FM type is expected. Mn atoms are replaced with Mg atoms at the

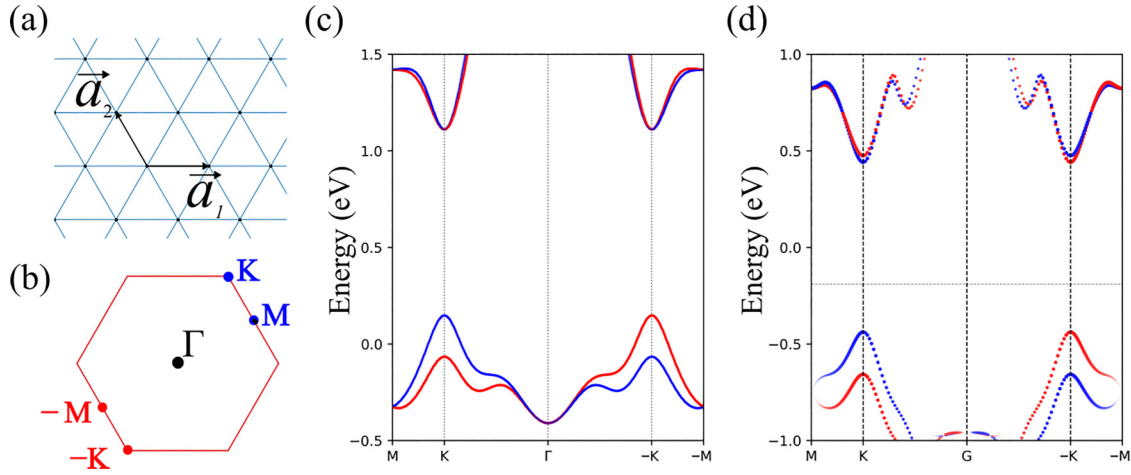


FIG. 3. (a) The triangular lattice formed by M atoms of monolayer MX_2 . (b) Band structure of the MoTe_2 monolayer obtained from the three-band TB model. Blue (red) color denotes the spin-down (spin-up) channel. (c) Projected band structure of the freestanding MoTe_2 monolayer from the DFT calculation. The shade of the blue (red) circle denotes the weight of the projection on the spin-down (spin-up) $\{d_{z^2}, d_{xy}, d_{x^2-y^2}\}$ orbitals.

nonmagnetic sites in type II and type IV to keep the valence state of the Mn^{2+} ions unchanged.

Dynamic stability and lattice mismatch are neglected for the MoTe_2/MnO hybrid since it is not the main point of this work. The structures of the AFM types are transformed from the FM MoTe_2/MnO primitive cell that has been relaxed in advance with the lattice constant 3.56 \AA [17]. In order to show that the effect of magnetic configuration on interlayer distance is negligible, the FM type, AFM type I, and AFM type III are relaxed with only the MoTe_2 layer fixed. The van der Waals interaction is included through the optB88-vdW method [32]. Further calculations are performed to study the effect of U_{eff} and Mn-Mo distance d on the valley splitting. The U_{eff} ranges from 4 to 7 eV with the “2+” valence state of Mn taken into account [33,34]. The d is tuned from 3.6 to 4.8 \AA . For one specific U_{eff} and d , the FM-type structures are partially relaxed through fixing the d and the pre-optimized MoTe_2 monolayer. The structures of the AFM types with the same U_{eff} and d are then constructed by enlarging the optimized unit cell of the FM type. Note that the Mn-Mo distances are the same in each AFM type. It implies the exactly total zero magnetization of the $\text{Mo}4d$ orbitals over the supercell. The systems listed in Tables III and IV keep semiconducting with Mn exhibiting about $5 \mu_B$ spin magnetic moment. A 20 \AA vacuum space along the z direction is applied to avoid periodic slab interaction in all DFT calculations. It is worth mentioning that the $\text{Mo}\{d_{z^2}, d_{xy}, d_{x^2-y^2}\}$ remain the dominant orbital components of the top valence band and the lowest conduction band at the two valleys in all cases.

III. RESULTS AND DISCUSSION

A. The valley degeneracy and the orbital-dependent valley splitting

In type I, \mathcal{T}_R symmetry reverses the spin z component and the sign of momentum, transforming the quantum state $\psi_{k,\uparrow}$ to $\psi_{-k,\downarrow}$ with a translation-induced phase shift. The structure

of the MoTe_2/MnO (111) hybrid is constructed, as shown in Fig. 4. As expected, the Kramer’s degeneracy remains throughout the whole BZ in the unfolded bands in Figs. 5(a) and 5(d). The valley splitting is prohibited in type I, where even the \mathcal{TS} is absent.

The two valleys stay degenerate in the unfolded bands in Figs. 5(b) and 5(e), although \mathcal{T}_R does not belong to the group of type II. The remaining degeneracy is protected by σ_v symmetry, which swaps green and red sites in Fig. 3(b). And the colors denoting spin z components commute as well since the spin z , as a pseudovector, is parallel to the vertical mirror plane. Thus, the system will change back to its initial configuration in real space. When it comes to reciprocal space, the K of the primitive BZ transforms to $-K$ after the σ_v operation in the BZ of the MoTe_2 monolayer. Yet, whether the states at the original valleys are degenerate depends on the states labeled by folded points from K and $-K$. As shown in Fig. 7(b), $\pm K$ fold to the corners of the smaller hexagonal BZ. Apparently, the nearest-neighbor corners are symmetric about the σ_v . Thus, the valley states originating from the MoTe_2 monolayer stay degenerate in the presence of the type-II AFM proximity effect.

In type III, the valley splitting is predicted to be induced in the absence of the two aforementioned special symmetries which ensure the valley degeneracy. Because no symmetry exists that reverts the spin and momentum simultaneously, the

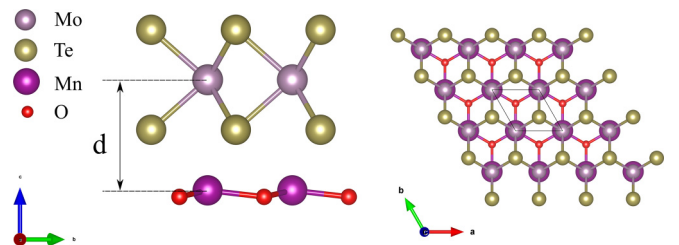


FIG. 4. The side and top views of the MoTe_2/MnO (111) hybrid.

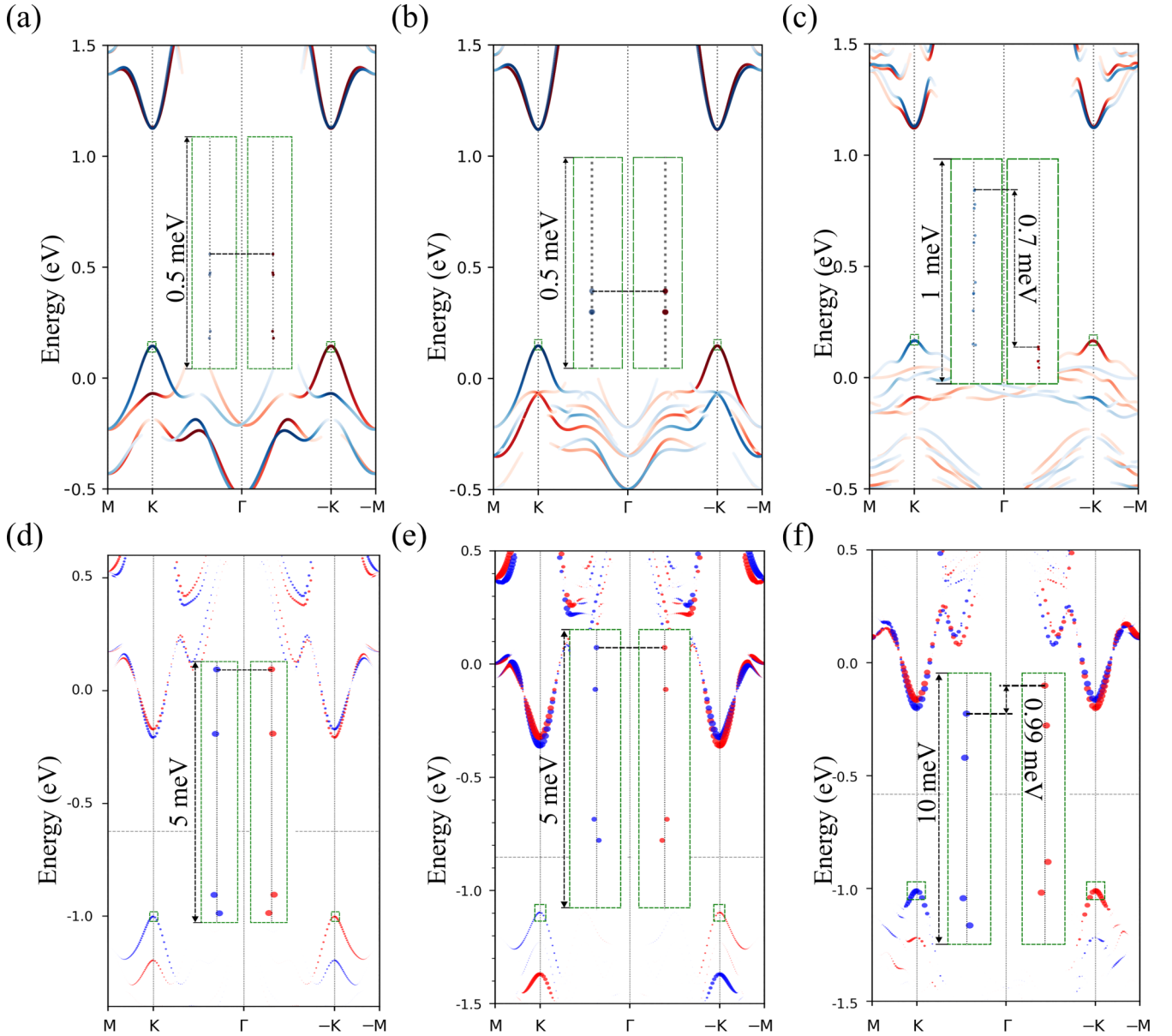


FIG. 5. Unfolded bands of the type I, II, and III hybrids. The green dashed frames represent amplified regions. (a),(c),(e) Unfolded bands from the TB models with $\vec{O} = (0.3, 0.1, 0.2)$ eV. The red/blue circles denote unfolded bands with spin \uparrow / \downarrow . For clarity, only the points with projection weight larger than 3% are plotted. (b),(d),(f) The unfolded bands from the DFT calculations with $U_{\text{eff}} = 4$ eV and $d = 3.6$ Å. The shade and size of the red/blue circles denote the unfolding weight multiplied by the weight of projection on Mo $\{d_{z^2}, d_{xy}, d_{x^2-y^2}\}$ with positive/negative component.

two valley states remain irrelevant to each other, regardless of which points $\pm K$ fold to. The numerical results verify the symmetry analyses above. A small valley splitting ~ 1 meV in the valence band is extracted from the TB model and the DFT calculation, as shown in Figs. 5(c) and 5(f). The main results are summarized in Table. I.

The dependence of the valley splitting in the AFM type III on the orbital-resolved proximity effect is further studied by tuning the modifier term in the TB model. The three matrix elements of \vec{O} change from 0.005 to 0.300 eV independently. The valley splitting in Fig. 6 reaches 5.7 meV at $\vec{O} = (0.300, 0.005, 0.300)$ eV and -4.7 meV at $\vec{O} = (0.300, 0.300, 0.160)$ eV. The nearly zero valley splitting ap-

pears in the region where the orbital energy shift is nonzero, as shown in Figs. 6(b) and 6(c). It is also found that a larger energy shift of d_{z^2} will lead to a more significant valley splitting when the valley splitting is nonzero.

TABLE I. Main results of the type I–III TMD/AFM hybrids.

	Special symmetry	Kramers' degeneracy	Valley degeneracy
Type I	\mathcal{T}_{tr}	preserved	preserved
Type II	σ_v	preserved	preserved
Type III	none	broken	broken

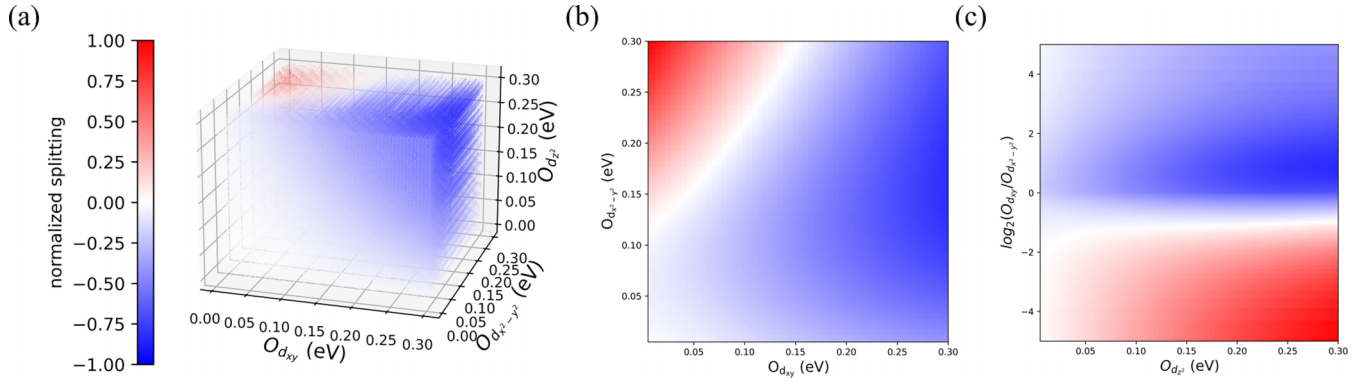


FIG. 6. The valley splitting with orbital-dependent energy shift from the TB model. The splitting of the two valleys [$\Delta_{tvb} = E_{tvb}(K, \downarrow) - E_{tvb}(-K, \uparrow)$] is normalized by its maximum 5.7 meV at $O = (0.300, 0.005, 0.300)$ eV. (b) The valley splitting with $O_{d_{xy}}$ and $O_{d_{x^2-y^2}} \cdot O_{d_{z^2}}$ is fixed at 0.300 eV. (c) The valley splitting with $O_{d_{z^2}}$ and $\log_2(O_{d_{xy}}/O_{d_{x^2-y^2}})$.

B. The mechanism of the valley degeneracy/splitting

In order to reveal the mechanism of the valley degeneracy/splitting in the three AFM types, the nondegenerate perturbation is adopted. Following the perturbation treatment, the dependence of the valley splitting on the orbital-resolved energy shift will be explained with the eigenstates extracted from the TB model.

The nondegenerate perturbation starts from the construction of the atomic basis consisting of Mo $\{d_{z^2}, d_{xy}, d_{x^2}\}$. In the supercell (SC) composed of the multiple identical primitive cells (PCs), the eigenstate is equivalent to that of the PC with the corresponding band and momentum index. The relationship between the momentum of the n_i th band of the PC and the m th band of the SC is given by

$$\vec{k}_i + \vec{G}_i \rightarrow \vec{\kappa}_i; |k_i, n_i\rangle \rightarrow |\kappa, m\rangle. \quad (3)$$

\vec{G}_i is the uniform reciprocal translation through which the n_i th band indexed by k_i in the Brillouin zone of the primitive cell (PBZ) folds to the m th band indexed by κ in the Brillouin zone of the supercell (SBZ). Considering that the PC only includes

one Mo atom, the unperturbed basis of the SC is expressed as

$$\begin{aligned} |k_i, n_i\rangle_\sigma &\longrightarrow |\kappa_i, m\rangle_\sigma = \frac{1}{\sqrt{N_p}} \sum_{\vec{R}_p} e^{i\vec{k}_i \cdot \vec{R}_p} \sum_{\alpha} c_{\alpha, \sigma}^{n_i}(\vec{k}_i) |\alpha\rangle_\sigma \\ &= \frac{1}{\sqrt{N_S}} \sum_{\vec{R}_S} e^{i\vec{k}_i \cdot \vec{R}_S} \frac{1}{\sqrt{N_\mu}} \\ &\quad \times \sum_{\alpha} \sum_{\mu} e^{i\vec{k}_i \cdot \vec{R}_\mu} c_{\alpha, \sigma}^{n_i}(\vec{k}_i) |\alpha, \mu\rangle_\sigma. \end{aligned} \quad (4)$$

N_p , N_S , and N_μ are the number of the PCs, SCs, and PCs, per one SC, respectively. The corresponding position is denoted by \vec{R}_p , \vec{R}_S , and \vec{R}_μ . The orbital and spin are denoted by α and σ . Note that the nondegenerate perturbation to the valley states is carried out due to the decoupled spin and orbital space. The first-order perturbation to the energy is expressed as

$$\begin{aligned} E_{n_i, \sigma}^{(1)}(\vec{k}_i = \vec{\kappa}) &= \langle \kappa, m | \hat{O} | \kappa, m \rangle_\sigma \\ &= \frac{1}{N_\mu} \sum_{\alpha} \sum_{\mu} \{ |c_{\alpha, \sigma}^{n_i}(\vec{\kappa})|^2 O_{\alpha, \mu, \sigma} \}. \end{aligned} \quad (5)$$

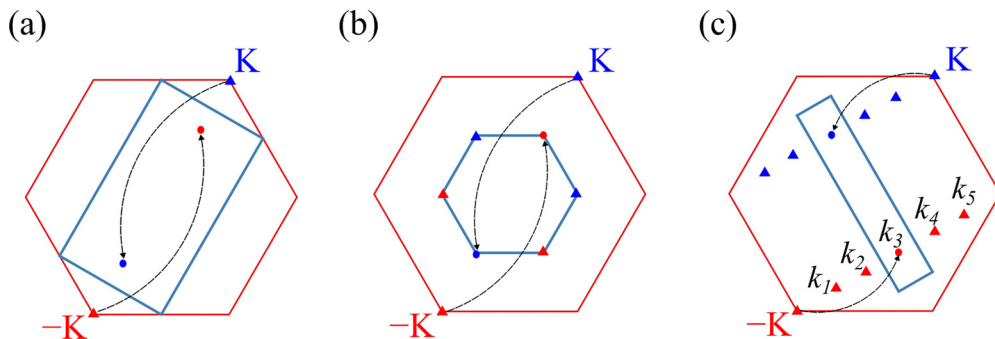


FIG. 7. The PBZ of the MoTe₂ monolayer and the SBZ of the three SCs. The sites which the points fold to in the SBZ are denoted by colored circles. The points folding to the same sites that the K or $-K$ folds to are denoted by colored triangles. (a) The SBZ of the AFM type I. Each k point in the SBZ corresponds to two points in the PBZ. (b) The SBZ of the AFM type II. Each k point in the SBZ corresponds to four points in the PBZ. (c) The SBZ of the AFM type III. $-K$ (K) and the other five inequivalent k points in the PBZ are folded to the k_3 ($-k_3$) in the SBZ.

TABLE II. The spin-up eigenstates of the valence band within the three-band basis at seven points of the PBZ. The eigenstate of the valence band at $-K$ is also listed. The zero energy is fixed at the maximum of the valence band.

	$ d_{z^2}, \uparrow\rangle$	$ d_{xy}, \uparrow\rangle$	$ d_{x^2-y^2}, \uparrow\rangle$	Energy (eV)
$ K, \uparrow\rangle$	0.000	-0.707	0.707i	-0.214
$ k_1, \uparrow\rangle$	0.654	0.278 + 0.368i	-0.541 + 0.261i	-0.404
$ k_2, \uparrow\rangle$	0.856	0.013 + 0.023i	-0.446 + 0.261i	-0.361
$ k_3, \uparrow\rangle$	0.880	-0.294 - 0.166i	-0.170 + 0.287i	-0.312
$ k_4, \uparrow\rangle$	0.856	-0.379 - 0.237i	0.234 + 0.111i	-0.361
$ k_5, \uparrow\rangle$	0.654	-0.330 - 0.410i	0.511 - 0.188i	-0.404
$ -K, \uparrow\rangle$	0.000	0.707	0.707i	0.000

Equation (5) yields the zero correction because the antiferromagnetism leads to the zero total energy shift over the whole SC. On the contrary, the nonzero first-order correction is obtained through the FM or ferrimagnetic proximity effect, where the net magnetic moment is nonzero. In the case of the second-order perturbation, the energy correction including the eigenstates indexed by different momentum in the PBZ may be nonzero due to the downsized BZ and the proximity effect.

It is given by

$$\begin{aligned} & \sum_{n'} E_{n'n',\sigma}^{(2)}(\vec{k}_i = \vec{K}, \vec{k}_i'; \vec{k}_i) \\ &= \sum_{n'} \frac{1}{N_\mu^2} \sum_{\alpha} \frac{|c_{\alpha,\sigma}^{n'}(\vec{k}_i')^* c_{\alpha,\sigma}^{n'}(\vec{k}_i) \sum_{\mu} e^{i(\vec{K}-\vec{k}_i')\cdot\vec{R}_\mu} O_{\alpha,\mu,\sigma}|^2}{E_n - E_{n'}}, \end{aligned} \quad (6)$$

with $E_n \neq E_{n'}$ and $\vec{k}_i' + \vec{G}_i = \vec{k}_i = \vec{K} + \vec{G}_i$. For the three AFM types in Fig. 2, all the k points involved in the perturbation are shown in Fig. 7. In the AFM type III, $-K$ (K) corresponds to the other five points folding to the k_3 ($-k_3$), as shown in Fig. 7(c). Note that for the correction $\sum_{n'} E_{n'n',\sigma}^{(2)}(\vec{k}_j = -\vec{K}, \vec{k}_j'; \vec{k}_j = -\vec{k})$, the sum over n' can be done with $\vec{k}_j' = -\vec{k}_i'$. Since $|-\vec{k}_i', n'\rangle_{\bar{\sigma}}$ is related to $|\vec{k}_i', n'\rangle_{\sigma}$ with the \mathcal{TS} , the sign and the absolute value of the second-order energy correction are the same for the two valley states. Thus, the valley degeneracy still holds. Up to the third order,

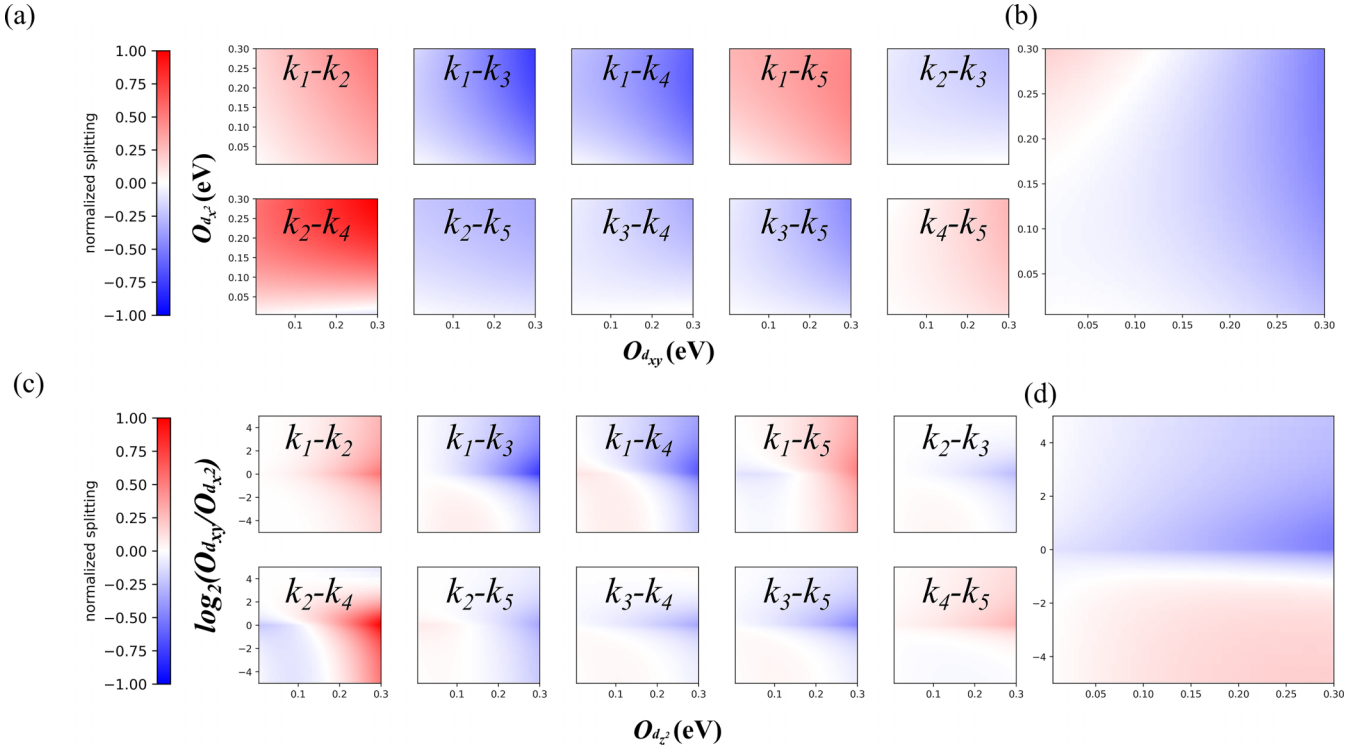


FIG. 8. The simulation of the Δ_{Ivb} based on the third-order perturbation. The eigenstates and the eigenenergies of the folding states are extracted from the TB results, as listed in Table II. The two k points in (a) and (c) represent the two intermediate states. The corresponding momentum is labeled in Fig. 7(c). In (a) and (b), the results are normalized by the maximal absolute value of the valley splittings from the 10 paths in (a). Similarly, the normalization in (c) and (d) is carried out with the valley splittings from the 10 paths in (c). (a) The partial contribution of the 10 paths to the valley splitting with $O_{d_{xy}}$ and $O_{d_{x^2-y^2}}$. The $O_{d_{z^2}}$ is fixed to be 0.300 eV. (c) The partial contribution of the 10 paths to the valley splitting with $\log_2(O_{d_{xy}}/O_{d_{x^2-y^2}})$ and $O_{d_{z^2}}$. (b), (d) The summation of the partial valley splitting in (a) and (c).

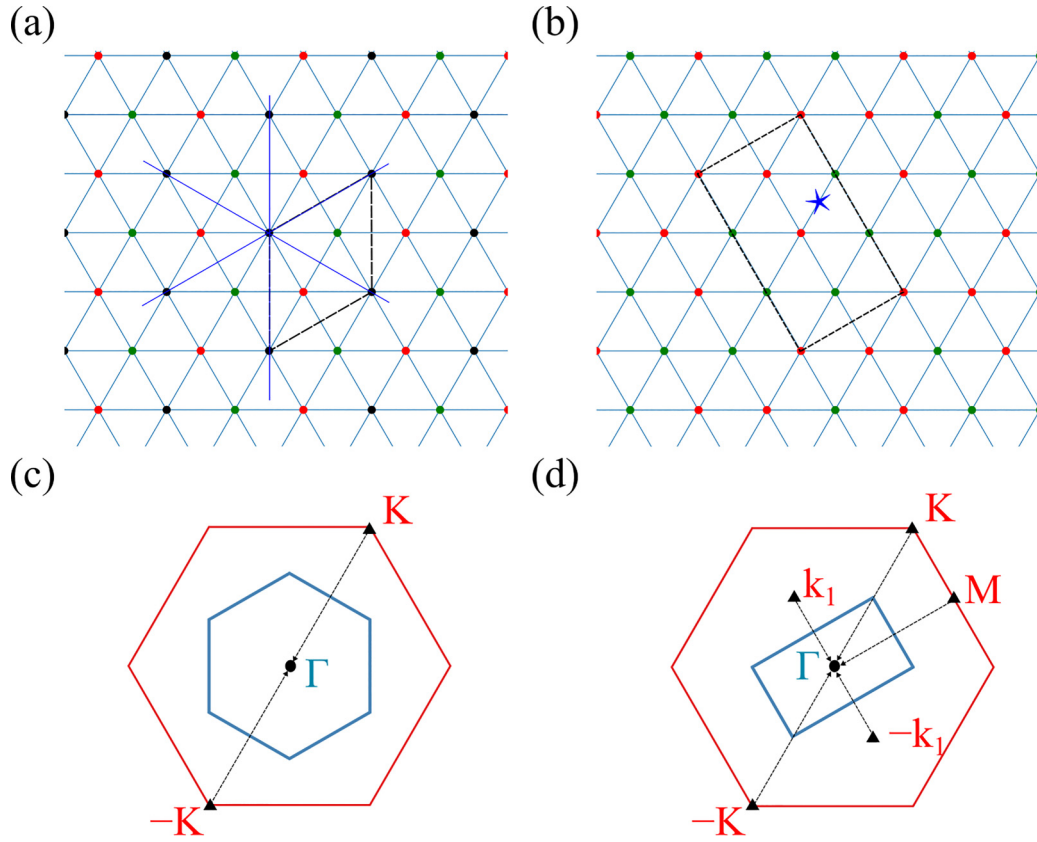


FIG. 9. The structures and the corresponding BZs of the AFM type-IV and type-V configurations. (a) The AFM type IV is symmetric about the three vertical mirror planes. (b) The AFM type V is unchanged under the inversion combined with time-reversal symmetry. The inversion center is labeled by the blue star. (c), (d) The BZ of AFM type-IV and type-V configuration. The points folding to the Γ are denoted by black triangles.

the expression is given by

$$\begin{aligned}
 E_{n_i, \sigma}^{(3)}(\vec{k}_i = \vec{K}) &= \sum_{p \neq n_i} \sum_{l \neq n_i} E_{n_i l} E_{l p} E_{p n_i} \\
 &= \sum_{p \neq n_i} \sum_{l \neq n_i} \frac{1}{E_{n_i} - E_l} \frac{1}{E_{n_i} - E_p} \\
 &\quad \times \langle K | \hat{O} | l \rangle_{\sigma} \langle l | \hat{O} | p \rangle_{\sigma} \langle p | \hat{O} | K \rangle_{\sigma}. \quad (7)
 \end{aligned}$$

One of the brackets in Eq. (7) is expressed as

$$\langle l | \hat{O} | p \rangle_{\sigma} = \frac{1}{N_{\mu}} \sum_{\alpha} c_{\alpha, \sigma}^l(\vec{k}_l)^* c_{\alpha, \sigma}^p(\vec{k}_p) \sum_{\mu} e^{i(\vec{k}_p - \vec{k}_l) \cdot \vec{R}_{\mu}} O_{\alpha, \mu, \sigma}. \quad (8)$$

In the case of the AFM type I or type II, the symmetry transformation S ($S = \mathcal{T}t_{\vec{R}}$ or σ_v) ensures the following relationship between the states with opposite momentum and spin:

$$\begin{aligned}
 \langle l | \hat{O} | p \rangle_{\sigma} &= \langle l | S^{\dagger} S \hat{O} S^{\dagger} S | p \rangle_{\sigma} \\
 &= \langle l_S | \hat{O} | p_S \rangle_{\bar{\sigma}}, \quad (9)
 \end{aligned}$$

where $|l_S\rangle_{\bar{\sigma}}$ and $|p_S\rangle_{\bar{\sigma}}$ are transformed states. It can be inferred from Eq. (9) that each pair of states (e.g., $|l\rangle_{\sigma}$ and $|l_S\rangle_{\bar{\sigma}}$) participating in the unfolding process in Fig. 7 contributes same

energy correction to the corresponding modified valley state in the AFM type I and type II. Specifically, states transform as $\hat{T}|l\rangle_{\sigma} = |-l\rangle_{\bar{\sigma}}$ in the AFM type I. Meanwhile, the \mathcal{TS} of the unperturbed system enforces $\langle l | \hat{O} | p \rangle_{\sigma} = -\langle -l | \hat{O} | -p \rangle_{\bar{\sigma}}^*$. As a result, the term $E_{n_i l} E_{l p} E_{p n_i} + E_{l n_i} E_{p l} E_{n_i p}$ in the summation over p and l is zero in the AFM type I. Without any special symmetry, a nonzero energy shift appears at two valleys in the AFM type III. Unlike the second-order term, the sign of the energy correction is opposite for the two valley states.

Based on the perturbation treatment above, the TB results in Fig. 6 will be discussed as follows. It is known that the eigenstates at the band edges of the valence bands are composed of the $\{d_{xy}, d_{x^2-y^2}\}$ orbitals. Thus, it is unusual that the Δ_{lvb} of type III depends on the energy shift of d_{z^2} , as shown in Fig. 6. In Table II, the orbital components of the spin-up valence band at K , $-K$ and k_i ($i = 1, \dots, 5$) are extracted through the three-band TB model. It is revealed that the large d_{z^2} component is included in the other five states participating in the third-order perturbation. As a result, the nominator relevant to the d_{z^2} component is nonzero in Eq. (7). On the other hand, the failure of the second-order perturbation is proved again due to the zero inner product of the d_{z^2} part in Eq. (6). The discussion above is further validated by simulation of the energy correction contributed

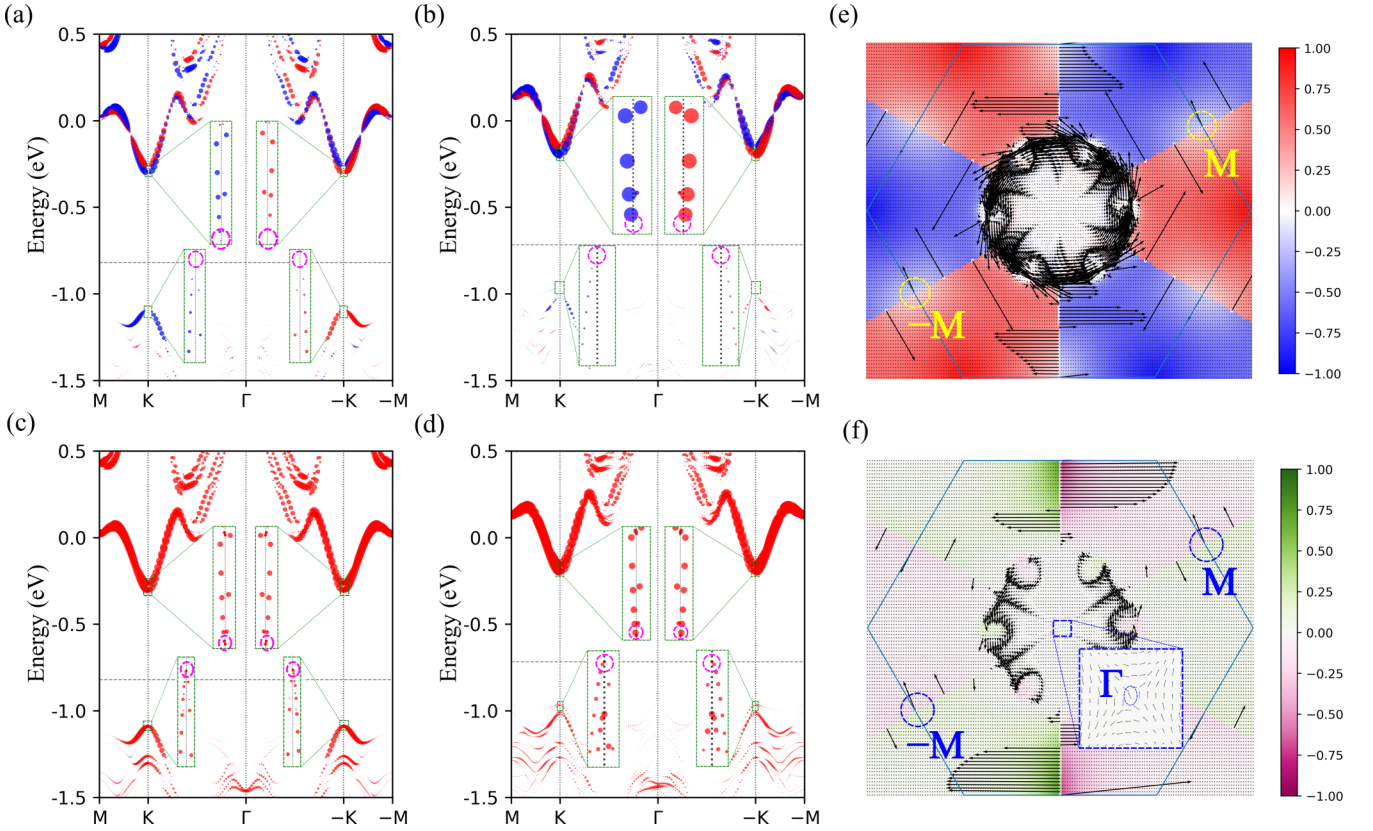


FIG. 10. (a)–(d) The unfolded bands of the AFM type-IV and type-V configurations. (a), (b) The size and the shade of the red (blue) circles denote the unfolded weight factorized by the weight of $\{d_{z^2}, d_{xy}, d_{x^2-y^2}\}$ with positive (negative) spin z component. (c), (d) The size and the shade of the red circles denote the unfolded weight multiplied by the projection on $\{d_{z^2}, d_{xy}, d_{x^2-y^2}\}$. (e), (f) The spin textures of the projected top valence band of the MoTe₂ monolayer in the reciprocal space. The shade of the colors denotes the projection weight of the specific orbitals with spin z component. The length of the arrow denotes the size of the projection weight of the specific orbitals with in-plane spin components. (e) The orbitals for projection are Mo $\{d_{xy}, d_{x^2-y^2}\}$. M and $-M$, which participate in the degenerate perturbation in type V, are labeled by yellow circles. (f) The orbitals for projection are Te p_x . The region centered at Γ is magnified with the blue dashed frame, where the nonzero intraplane spin component at Γ is labeled by a blue circle. The spin texture projecting on Te p_y reflects similar property, only differing by the orientation of the spin. Thus, the projection on p_y is not included.

from 10 perturbation paths, as shown in Fig. 8. The major features of the accumulative effect in Figs. 8(b) and 8(d) agree well with the TB results. To sum up, the third-order perturbation reveals how the valley splitting happens and depends on the orbital-resolved proximity effect.

It should be noted that the well-defined valley states will no longer exist if the two valley points K and $-K$ fold to the same point Γ . The AFM type-IV and type-V configurations are constructed as the negative examples. In both types, the two valley states fold to Γ , as shown in Fig. 9. According to the TB model, the valley degeneracy and valley splitting are predicted in the AFM type IV and type V, respectively. However, the nearly zero weight of the band projection on the spin z component of $\{d_{z^2}, d_{xy}, d_{x^2-y^2}\}$ occurs at K and $-K$ in the DFT calculation, as shown in Figs. 10(a) and 10(b). Meanwhile, the weight of the band projection on $\{d_{z^2}, d_{xy}, d_{x^2-y^2}\}$ at the two valleys is nonzero in Figs. 10(c) and 10(d). It indicates that the two valley states $|K, \downarrow\rangle$ and $|-K, \uparrow\rangle$ mix with each other after the introduction of the AFM proximity effects

in Figs. 9(a) and 9(b). In order to explain the anomalous results, the degenerate perturbation is adopted. The interested subspace is spanned by two valley states $|K, \downarrow\rangle$ and $|-K, \uparrow\rangle$. Up to the second-order degenerate perturbation through the Lowdin partitioning equation [35], the off-diagonal matrix element between two valley states is expressed as

$$\lambda = H_{K,-K}^{(2)} = \frac{1}{2} \sum_l \hat{O}_{K,k_l} \hat{O}_{k_l,-K} \left[\frac{1}{E_K - E_l} + \frac{1}{E_{-K} - E_l} \right]. \quad (10)$$

λ will become nonzero under two conditions. First, there are points other than K and $-K$ folding to the Γ . Second, common orbital components exist in $\{|k_l\rangle, -|k_l\rangle\}$ and $\{|K, \downarrow\rangle, |-K, \uparrow\rangle\}$. These orbital components of the $\{|k_l\rangle, -|k_l\rangle\}$ are further required to include both spin channels. Then, the eigenstates in the subspace spanned by two valley states will be in the form of $|K, \downarrow\rangle + \frac{\lambda^*}{|\lambda|} |-K, \uparrow\rangle$ no matter how small the λ is. Consequently, the expecta-

tion value of the spin operator is zero with an arbitrary spin-quantization axis.

Based on the analysis above, the spin texture of the top valence band in the MoTe₂ monolayer is extracted to check the orbital and spin components. As shown in the yellow circled region of Fig. 10(e), the projection weight of the $\{d_{xy}, d_{x^2-y^2}\}$ with in-plane spin direction is nonzero at M . Although the $\{d_{xy}, d_{x^2-y^2}\}$ component becomes zero at Γ , a tiny but nonzero projection on Te $\{p_x, p_y\}$ has been found at Γ , as shown Fig. 10(f). The finite in-plane spin component means both spin-up and spin-down channels are contained for the projected orbitals. Thus, the folded state $|M\rangle$ drives the mixture of the two valley states in the AFM type V. In type IV, the mixed states are caused by the folded state $|\Gamma\rangle$. That is why the nearly zero weight of projection on Mo $\{d_{z^2}, d_{xy}, d_{x^2-y^2}\}$ with the spin z component projection in the DFT calculation of the

TABLE III. The top valence-band splitting V_{vs} and the lowest conduction-band splitting C_{vs} of the FM type under different U_{eff} values. The splittings are in the unit of meV. The atomic sites of the oxygen in each structure with fixed Mn-Mo distance under specific U_{eff} have been optimized.

U_{eff} (eV)	7		6		5		4	
	V_{vs}	C_{vs}	V_{vs}	C_{vs}	V_{vs}	C_{vs}	V_{vs}	C_{vs}
3.6	71.3	112.2	79.3	122.9	87.8	135.0	96.6	148.5
4.0	33.4	60.5	38.0	65.6	43.5	71.4	50.3	79.7
4.4	7.4	27.8	8.9	29.8	11.1	32.5	16.1	40.6
4.8	-4.0	11.8	-3.9	13.0	-2.3	15.3	2.8	21.3

AFM type IV and V. The problem is naturally avoided in the three-band TB model because the spin space is decoupled with

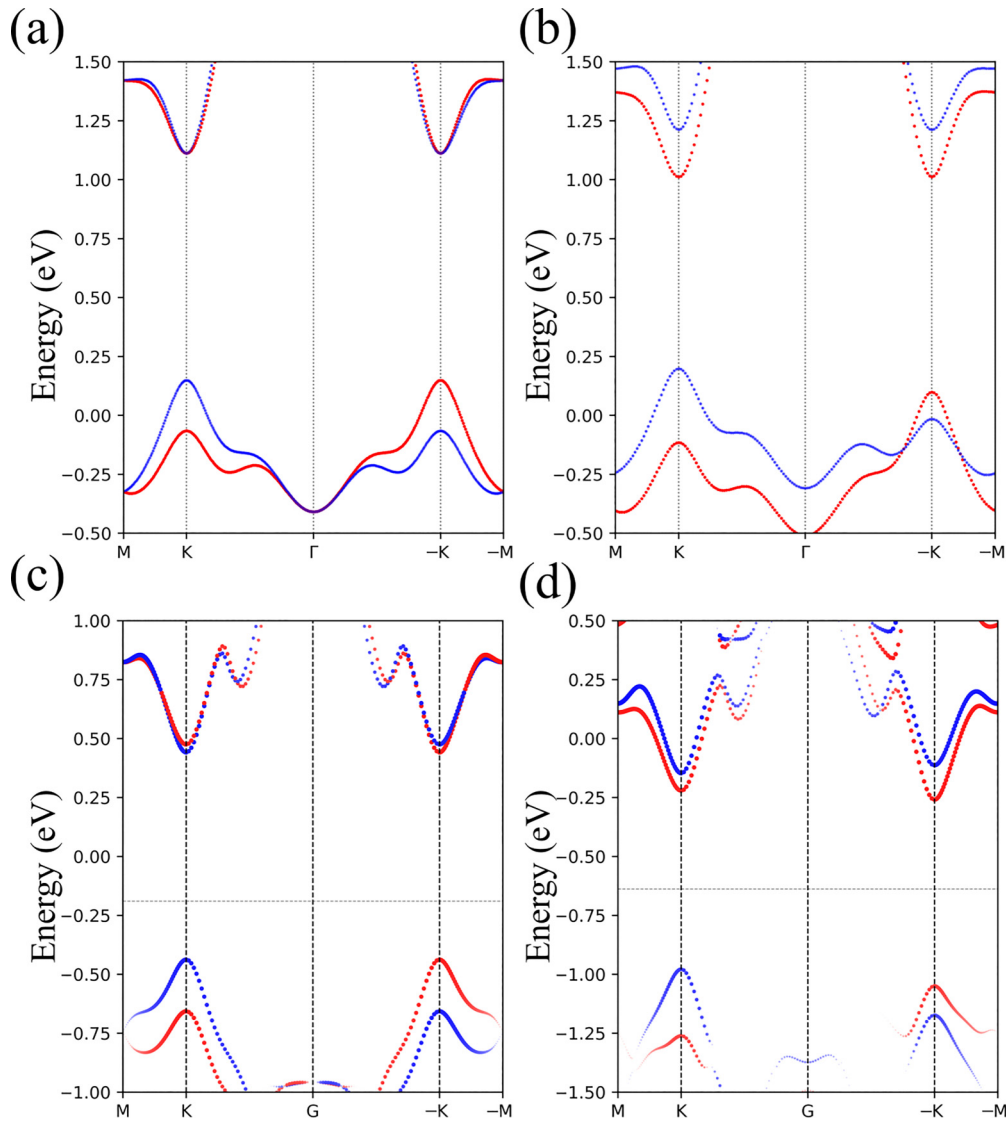


FIG. 11. (a), (b) The band structures from the TB model. The on-site energy shift is (a) zero and (b) $\vec{D} = -(0.100, 0.050, 0.050)$ eV. Red/blue denotes the spin-up/spin-down channel. (c), (d) The band structures from the DFT calculations of (c) the freestanding MoTe₂ monolayer and (d) the MoTe₂/MnO hybrids with $d = 3.6$ Å and $U_{\text{eff}} = 4$ eV. The magnetic moment of the Mn²⁺ aligns along the direction normal to the plane. Red/blue circles represent the projected bands. The shade denotes the weight of projection on Mo $\{d_{z^2}, d_{xy}, d_{x^2-y^2}\}$ with spin up/spin down.

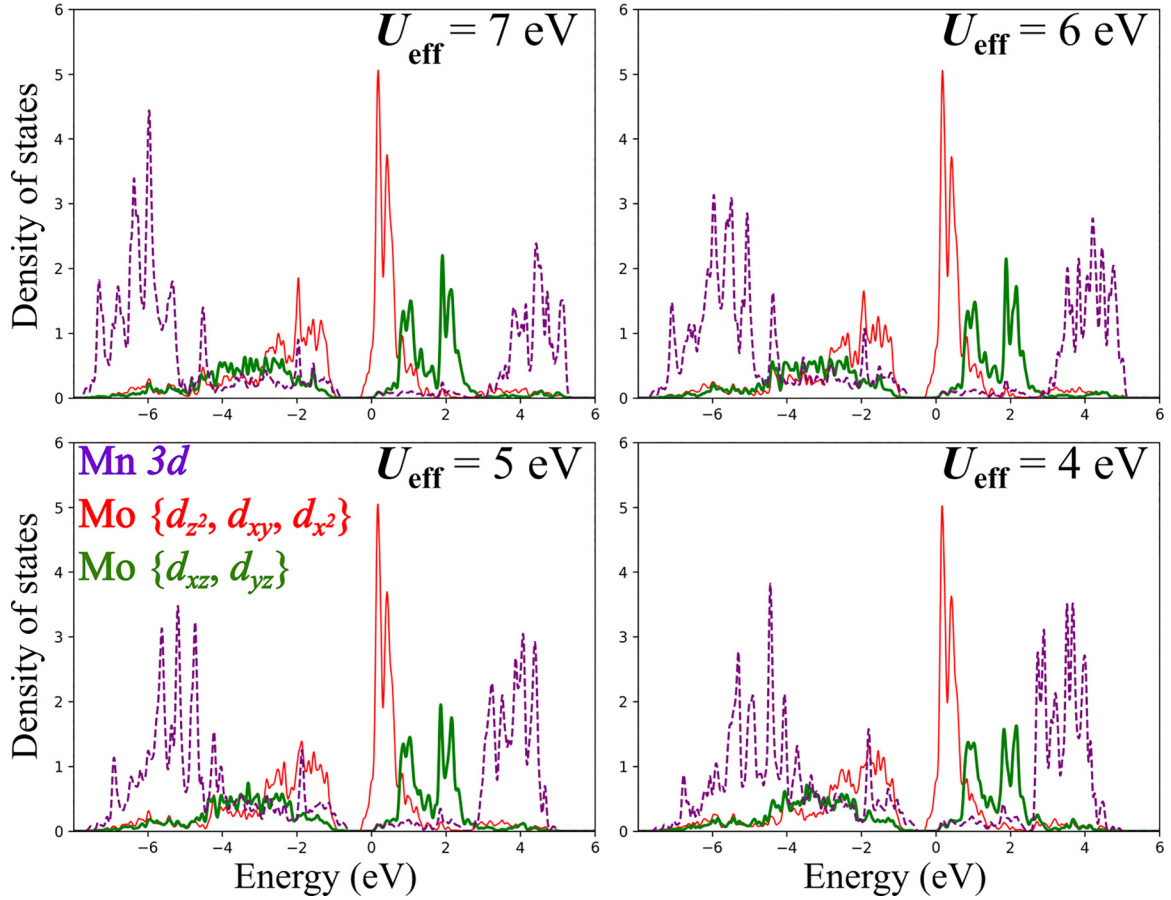


FIG. 12. The PDOS on Mn $3d$ orbitals and Mo $4d$ orbitals with $d = 3.6$ Å under different U_{eff} .

the orbital space, which excludes the degenerate perturbation. Thus, the construction of the SC where K and $-K$ fold to the Γ should be avoided since the second-order degenerate perturbation couples the two well-defined valley states.

C. The effect of the interlayer distance and U_{eff} on the valley splitting

Although the hybrid systems are novel due to the unstable MnO (111) monolayer, instructive results are also provided for engineering functional materials. In order to investigate the method of controlling the valley splitting, the effects of the d and U_{eff} on the valley splitting have been studied through the DFT calculations. In spite of influence from the magnetic configuration, only a small difference less than 0.1 Å is found in the relaxed FM type and in the AFM type I and type III with $d = 4.754, 4.807, 4.727$ Å, respectively, under $U_{\text{eff}} = 4$ eV. The AFM type II is not included because of the additional effect of atomic substitution. Thus, the magnetic configuration effect on the interlayer distance is neglected in the following calculations.

The properties of the FM types are discussed first. Compared to the freestanding MoTe_2 monolayer in Fig. 11(c), the spin-up Mo bands within the low-energy region decrease in Fig. 11(d) due to the magnetic proximity effect from the spin-up magnetic moment of the Mn. The DFT results are consistent with the TB results in Figs. 11(a) and 11(b), where the on-site energy shift is zero in (a) and negative for spin-up channel in (b). On condition that the effective exchange field

is provided by spin-up magnetic moment of the Mn, the main results of FM-type MoTe_2/MnO hybrids under different U_{eff} and d are summarized in Table III. The top valence-band splitting (V_{vs}) and the lowest conduction-band splitting (C_{vs}) at the two valleys tend to decrease as the U_{eff} increases. The C_{vs} keeps decreasing, while the V_{vs} decreases until the sign flips when the d increases from 4.4 to 4.8 Å. Note that the proximity effect results from the overlap between the Mo $4d$ orbitals and Mn $3d$ orbitals. That is why the Mo orbitals with spin parallel to the magnetic moment of the Mn tend to be lowered in Fig. 11(d) after the introduction of magnetic proximity effect. As a result, a larger overlap implies a larger magnetization of Mo, which means a larger valley splitting. When U_{eff} decreases, Mn $3d$ orbitals tend to be more delocalized. Then, the magnetization of the Mo $4d$ orbitals strengthens due to the larger overlap from the more extensive $3d$ wave function. It is reflected from the enhanced hybridization between the Mn $3d$ orbitals and Mo $4d$ orbitals through the projected density of states (PDOS) in Fig. 12. Similarly, the valley splitting of the FM type decreases as the d increases from 3.6 to 4.4 Å with fixed U_{eff} . When the d is up to 4.8 Å, the magnetization from the direct overlap is significantly suppressed. On the other hand, the superexchange-like process (SE) originating from the kinetic energy of electrons lowers the Mo $4d$ orbitals with the spin antiparallel to the magnetic moment of Mn. The mechanism of antiferromagnetism can be physically described by the virtual hopping process involving the Mo $4d$ and the Mn $3d$ orbitals via Te $5p$ orbitals [36].

TABLE IV. The top valence-band splitting V_{vs} with $d = 3.6 \text{ \AA}$.

$U_{\text{eff}}(\text{eV})$	7	6	5	4
$V_{vs}(\text{meV})$	-0.32	-0.43	-0.64	-0.99

Such high-order term from the perturbation scales as $\frac{t_{\text{eff}}^2}{U}$. The effective hopping $t_{\text{eff}} = \frac{t_{dp}^{\text{Mn}} t_{dp}^{\text{Mo}}}{\Delta}$ contains the charge transfer energy Δ , the hopping term for Mn $3d$ -Te $5p$, and the hopping term for Mo $4d$ -Te $5p$. Thus, the magnetization from the SE is negligible in the case of small d compared to that from the direct overlap. Note that the SE decreases much more slowly than direct overlap due to the fixed Mo-Te and slowly elongated Mn-Te distances as d increases. When the increasing d is large enough, the direct overlap decays exponentially and tends to be zero. The AFM SE subsequently dominates the magnetization of Mo. That is why the V_{vs} becomes negative in the case of $d = 4.8 \text{ \AA}$ for $U_{\text{eff}} = 7, 6, 5 \text{ eV}$. By comparison, the C_{vs} remains positive. The difference results from the specific orbital components. As the main orbital component of the lowest conduction band at the valleys, Mo d_{z^2} enables more direct overlap than the in-plane distributed Mo $\{d_{xy}, d_{x^2}\}$ orbitals.

Analogous to the discussion above, the V_{vs} in the AFM type III shares a similar dependence on the d and U_{eff} . The V_{vs} of type IV is extracted under different U_{eff} . Only the cases with $d = 3.6 \text{ \AA}$ are shown because the splittings in other insulating cases are smaller by nearly an order of magnitude. As listed in Table IV, V_{vs} increases with the decreasing U_{eff} . According to the analysis in Sec. III B, the size of the V_{vs} partially depends on the absolute value of each element in \vec{O} . Meanwhile, these spin-up orbital-resolved energy shifts in the AFM type III are the same as those in the FM type. It is ensured by the aforementioned construction of the AFM configurations. Consequently, a similar trend of the U_{eff} -dependent valley splitting in the FM type is expected to appear in the AFM type III, as shown in Table IV. With the discussion above, tuning the magnetization of Mo is the key to manipulate the valley splitting in both FM and AFM types. Controllable magnetization can be obtained through interlayer distance and suitable magnetic layers with extensive or localized orbitals in real materials.

IV. CONCLUSION

A three-band tight-binding model is extended to investigate the proximity effect of the intraplane AFM configurations. Two specific AFM types are predicted to preserve valley degeneracy resulting from the \mathcal{T}_R or σ_v symmetry. Another type with trivial symmetries unsurprisingly breaks the valley degeneracy. Through symmetry analysis, valley degeneracy/splitting in the three particular systems is well explained, which agrees with the unfolded bands from the TB model and DFT calculations. The effect of the orbital-dependent energy shift is investigated with the TB model as well. The mechanism is revealed through the nondegenerate perturbation theory. Further constraints of the SC are proposed based on the degenerate perturbation. Beyond the analytical study, the magnetization of the Mo, which depends on U_{eff} and interlayer distance d , is found to be effective to tune the valley splitting in real materials.

In the present paper, the extended TB model captures the main features of the composite systems within the low-energy region, which may pave the way to study the corresponding quantum states at valleys. It provides a simple but accurate enough pathway to describe the low-energy physics for valleytronics, especially in nanoscale systems. Invalid cases where the well-defined valley states disappear can be avoided with the proposed constraints of the AFM configurations. We believe that these results are instructive for the flexible manipulation of valley states. With a combination of valleytronics and spintronics, the valley-splitting states and valley-degenerate states can be switched by tuning the magnetic structure of the proximity layer. Furthermore, it is known that the number of AFM insulators is much more than that of the FM ones. Thus, the results enormously expand the prospect of proximity for valley polarization.

ACKNOWLEDGMENTS

This work was supported by the National Key R&D Program of China (Grant No. 2022YFA1402401) and the National Natural Science Foundation of China (Grant No. 11521404). Computational resources were supported by the Center for High Performance Computing at Shanghai Jiao Tong University.

- [1] D. Xiao, W. Yao, and Q. Niu, Valley-Contrasting Physics in Graphene: Magnetic Moment and Topological Transport, *Phys. Rev. Lett.* **99**, 236809 (2007).
- [2] W. Yao, D. Xiao, and Q. Niu, Valley-dependent optoelectronics from inversion symmetry breaking, *Phys. Rev. B* **77**, 235406 (2008).
- [3] T. Cao, G. Wang, W. Han, H. Ye, C. Zhu, J. Shi, Q. Niu, P. Tan, E. Wang, B. Liu, and J. Feng, Valley-selective circular dichroism of monolayer molybdenum disulfide, *Nat. Commun.* **3**, 887 (2012).
- [4] D. Xiao, G.-B. Liu, W. Feng, X. Xu, and W. Yao, Coupled Spin and Valley Physics in Monolayers of MoS_2 and Other Group-VI Dichalcogenides, *Phys. Rev. Lett.* **108**, 196802 (2012).
- [5] K. F. Mak, C. Lee, J. Hone, J. Shan, and T. F. Heinz, Atomically Thin MoS_2 : A New Direct-Gap Semiconductor, *Phys. Rev. Lett.* **105**, 136805 (2010).
- [6] H. Zeng, J. Dai, W. Yao, D. Xiao, and X. Cui, Valley polarization in MoS_2 monolayers by optical pumping, *Nat. Nanotechnol.* **7**, 490 (2012).
- [7] K. F. Mak, K. He, J. Shan, and T. F. Heinz, Control of valley polarization in monolayer MoS_2 by optical helicity, *Nat. Nanotechnol.* **7**, 494 (2012).
- [8] K. F. Mak, K. L. McGill, J. Park, and P. L. McEuen, The valley Hall effect in MoS_2 transistors, *Science* **344**, 1489 (2014).
- [9] J. R. Schaibley, H. Yu, G. Clark, P. Rivera, J. S. Ross, K. L. Seyler, W. Yao, and X. Xu, Valleytronics in 2D materials, *Nat. Rev. Mater.* **1**, 16055 (2016).

- [10] J. Lee, K. F. Mak, and J. Shan, Electrical control of the valley Hall effect in bilayer MoS₂ transistors, *Nat. Nanotechnol.* **11**, 421 (2016).
- [11] A. Splendiani, L. Sun, Y. Zhang, T. Li, J. Kim, C.-Y. Chim, G. Galli, and F. Wang, Emerging photoluminescence in monolayer MoS₂, *Nano Lett.* **10**, 1271 (2010).
- [12] A. C. Dias, H. Bragança, H. Zeng, A. L. A. Fonseca, D.-S. Liu, and F. Qu, Large room-temperature valley polarization by valley-selective switching of exciton ground state, *Phys. Rev. B* **101**, 085406 (2020).
- [13] Y. Li, J. Ludwig, T. Low, A. Chernikov, X. Cui, G. Arefe, Y. D. Kim, A. M. van der Zande, A. Rigosi, H. M. Hill, S. H. Kim, J. Hone, Z. Li, D. Smirnov, and T. F. Heinz, Valley Splitting and Polarization by the Zeeman Effect in Monolayer MoS₂, *Phys. Rev. Lett.* **113**, 266804 (2014).
- [14] D. MacNeill, C. Heikes, K. F. Mak, Z. Anderson, A. Kormányos, V. Zólyomi, J. Park, and D. C. Ralph, Breaking of Valley Degeneracy by Magnetic Field in Monolayer MoSe₂, *Phys. Rev. Lett.* **114**, 037401 (2015).
- [15] G. Aivazian, Z. Gong, A. M. Jones, R.-L. Chu, J. Yan, D. G. Mandrus, C. Zhang, D. Cobden, W. Yao, and X. Xu, Magnetic control of valley pseudospin in monolayer WSe₂, *Nat. Phys.* **11**, 148 (2015).
- [16] K. L. Seyler, D. Zhong, B. Huang, X. Linpeng, N. P. Wilson, T. Taniguchi, K. Watanabe, W. Yao, D. Xiao, M. A. McGuire, K.-M. C. Fu, and X. Xu, Valley manipulation by optically tuning the magnetic proximity effect in WSe₂/CrI₃ heterostructures, *Nano Lett.* **18**, 3823 (2018).
- [17] J. Qi, X. Li, Q. Niu, and J. Feng, Giant and tunable valley degeneracy splitting in MoTe₂, *Phys. Rev. B* **92**, 121403(R) (2015).
- [18] L. Ciorciaro, M. Kroner, K. Watanabe, T. Taniguchi, and A. Imamoglu, Observation of Magnetic Proximity Effect Using Resonant Optical Spectroscopy of an Electrically Tunable MoSe₂/CrBr₃ Heterostructure, *Phys. Rev. Lett.* **124**, 197401 (2020).
- [19] G. Yang, J. Li, H. Ma, Y. Yang, C. Li, X. Mao, and F. Yin, Induced valley splitting in monolayer MoS₂ by an antiferromagnetic insulating CoO (111) substrate, *Phys. Rev. B* **98**, 235419 (2018).
- [20] G.-B. Liu, W.-Y. Shan, Y. Yao, W. Yao, and D. Xiao, Three-band tight-binding model for monolayers of group-VIB transition metal dichalcogenides, *Phys. Rev. B* **88**, 085433 (2013).
- [21] Guo-Yi Zhu, Ziqiang Wang, and Guang-Ming Zhang, Two-dimensional topological superconducting phases emerged from d-wave superconductors in proximity to antiferromagnets, *Europhys. Lett.* **118**, 37004 (2017).
- [22] W. Ku, T. Berlijn, and C.-C. Lee, Unfolding First-Principles Band Structures, *Phys. Rev. Lett.* **104**, 216401 (2010).
- [23] V. Popescu and A. Zunger, Extracting E versus \vec{k} effective band structure from supercell calculations on alloys and impurities, *Phys. Rev. B* **85**, 085201 (2012).
- [24] M. Farjam, Projection operator approach to unfolding supercell band structures, *arXiv:1504.04937*.
- [25] H. Huang, F. Zheng, P. Zhang, J. Wu, B.-L. Gu, and W. Duan, A general group theoretical method to unfold band structures and its application, *New J. Phys.* **16**, 033034 (2014).
- [26] G. Kresse and J. Furthmüller, Efficiency of *ab initio* total energy calculations for metals and semiconductors using a plane-wave basis set, *Comput. Mater. Sci.* **6**, 15 (1996).
- [27] G. Kresse and J. Furthmüller, Efficient iterative schemes for *ab initio* total-energy calculations using a plane-wave basis set, *Phys. Rev. B* **54**, 11169 (1996).
- [28] P. E. Blöchl, Projector augmented-wave method, *Phys. Rev. B* **50**, 17953 (1994).
- [29] J. P. Perdew, K. Burke, and M. Ernzerhof, Generalized Gradient Approximation Made Simple, *Phys. Rev. Lett.* **77**, 3865 (1996).
- [30] J. P. Perdew, K. Burke, and M. Ernzerhof, Generalized Gradient Approximation Made Simple [Phys. Rev. Lett. 77, 3865 (1996)], *Phys. Rev. Lett.* **78**, 1396(E) (1997).
- [31] S. L. Dudarev, G. A. Botton, S. Y. Savrasov, C. J. Humphreys, and A. P. Sutton, Electron-energy-loss spectra and the structural stability of nickel oxide: An LSDA + *U* study, *Phys. Rev. B* **57**, 1505 (1998).
- [32] J. c. v. Klimeš, D. R. Bowler, and A. Michaelides, Van der Waals density functionals applied to solids, *Phys. Rev. B* **83**, 195131 (2011).
- [33] V. I. Anisimov, J. Zaanen, and O. K. Andersen, Band theory and Mott insulators: Hubbard *U* instead of stoner *I*, *Phys. Rev. B* **44**, 943 (1991).
- [34] S. Mandal, K. Haule, K. M. Rabe, and D. Vanderbilt, Systematic beyond-DFT study of binary transition metal oxides, *npj Comput. Mater.* **5**, 115 (2019).
- [35] R. Winkler, *Spin-orbit Coupling Effects in Two-Dimensional Electron and Hole Systems* (Springer, Heidelberg, 2003).
- [36] P. W. Anderson, Antiferromagnetism. Theory of superexchange interaction, *Phys. Rev.* **79**, 350 (1950).